Extension of the Binding Motif of the Sin3 Interacting Domain of the Mad Family Proteins[†,‡]

Hugo van Ingen,[§] Edwin Lasonder,[||] Jacobus F. A. Jansen,[§] Anita M. Kaan,[||] Christian A. E. M. Spronk,[§,⊥]
Henk G. Stunnenberg,[||] and Geerten W. Vuister*[,§]

*Departments of Biophysical Chemistry and Molecular Biology, NSRIM Center, University of Nijmegen, Toernooiveld 1,
6525 ED Nijmegen, The Netherlands*

Received September 2, 2003; Revised Manuscript Received November 5, 2003

ABSTRACT: Sin3 forms the scaffold for a multiprotein corepressor complex that silences transcription via the action of histone deacetylases. Sin3 is recruited to the DNA by several DNA binding repressors, such as the helix−loop−helix proteins of the Mad family. Here, we elaborate on the Mad−Sin3 interaction based on a binding study, solution structure, and dynamics of the PAH2 domain of mSin3 in complex to an extended Sin3 interacting domain (SID) of 24 residues of Mad1. We show that SID residues Met7 and Glu23, outside the previously defined minimal binding motif, mediate additional hydrophobic and electrostatic interactions with PAH2. On the basis of these results we propose an extended consensus sequence describing the PAH2−SID interaction specifically for the Mad family, showing that residues outside the hydrophobic core of the SID interact with PAH2 and modulate binding affinity to appropriate levels.

Sin3 is a ubiquitous, highly conserved protein involved in repression of gene transcription. Sin3 acts as a corepressor and is recruited to the DNA by various DNA binding repressors. Gene silencing is brought about by its association with histone deacetylases (HDAC) (*1*−*3*), which deacetylate the core histones resulting in a repressed state of the chromatin (*4*, *5*). Sin3 is thought to act as a scaffold protein for the corepressor complex, recruiting not only HDAC1/HDAC2 but also histone binding proteins RbAp46/RbAp48, Sin3 associated proteins SAP18/SAP30, and the recently identified Sds3, SAP180, and SAP130 to form a large multimeric active repression complex (*1*−*3*, *6*−*8*).

Sin3 contains at least three stretches of about 80 residues, subsequently denoted as PAH1, PAH2, and PAH3 (*p*oly*a*mphipathic *h*elix domains), which are highly conserved in different forms of the Sin3 protein. These domains are suggested to be the protein−protein interaction domains by which Sin3 fulfils its role as a scaffold. However, thus far the PAH2 domain has mainly been identified as the interaction domain, whereas interactions involving the PAH1 and PAH3 domains are much more tentative. Moreover, for a number of interactors, regions other than the PAH domains were shown to be essential for binding as in the case of HDAC (*2*), Sds3 (*7*), p53 (*9*), and MeCP2 (*10*, *11*).

A large number of repressors have been identified that by direct interaction with Sin3 recruit the corepressor complex, one of which is Mad1 (*12*, *13*), a basic region/helix−loop−helix/leucine zipper (bHLHZip) transcription factor. Mad1 belongs to a family of four proteins (Mad1, Mxi1, Mad3, and Mad4), which are part of the Myc/Max/Mad network involved in cell cycle regulation. Both the Mad proteins and the proto-oncogene product Myc bind E-box DNA sequences (CACGTG) and heterodimerize with Max through their bHLHZip domains. While Myc-Max promotes cell proliferation and transformation and is implicated in tumorigenesis, Mad-Max is found at high levels in differentiating cells and represses a subset of target genes of Myc (*14*−*16*). Abrogation of Mad-mediated repression has been linked to the development of promyelocytic leukemia (*17*), and knockout studies implicated Mxi1 to be a potential tumor suppressor (*18*).

The repressive function of the Mad family depends on their interaction with the PAH2 domain of Sin3 through a short amphipathic helix located at their N-terminus termed SID (*19*, *20*) for Sin3 interacting domain. Recently, a molecular basis has been provided for understanding this interaction by the NMR structures of the Mad1−SID Sin3−PAH2 complex (*21*, *22*). In the study of Brubaker et al. (*21*) the PAH2 domain of the A-form of the mammalian Sin3, mSin3A, was used together with a SID of 16 residues (residues 6−21), which will subsequently be denoted as PAH2^{A}−SID16. The study of Spronk et al. (*22*) used the PAH2 domain of the B-form of mammalian Sin3, mSin3B, and a SID of 13 residues (residues 8−20), subsequently denoted as PAH2^{B}−SID13. The PAH domains of mSin3A

[†] Financial support was provided by the Dutch Organization for Scientific Research, NWO (JC 99-03).

[‡] The coordinates of the structures were deposited in the RCSB Protein Data Bank under PDB accession number 1PD7. The chemical shifts of the extended SID and chemical shifts and ^{15}N relaxation data of the PAH2^{B} domain are deposited in the BioMagResBank under BMRB accession numbers 5457 and 5808, respectively.

* Corresponding author. Phone: +31-24-365-2321. Fax: +31-24-365-2112. E-mail: vuister@nmr.kun.nl.

[§] Department of Biophysical Chemistry, NSRIM Center, University of Nijmegen.

[||] Department of Molecular Biology, NCMLS, University of Nijmegen.

[⊥] Current address: Center for Molecular and Biomolecular Informatics (CMBI), NSRIM Center, University of Nijmegen, Toernooiveld 1, 6525 ED Nijmegen, The Netherlands.

10.1021/bi0355645 CCC: $27.50

and mSin3B share ∼60−70% sequence identity, and at present, there is little knowledge about any functional differences between these two forms of mSin3. In both studies, the PAH2 domain is folded as a four-helix bundle, and the amphipathic helix of the SID is wedged between helix α1 and helix α2 of PAH2 at angle of ∼45°, a folding motif denoted as the "wedged helical bundle" (*22*).

On the basis of their structure, multiple sequence alignments, and mutation data, Brubaker et al. proposed a consensus sequence for a 13-residue minimal SID, showing that interaction is mainly mediated by the hydrophobic surface of the amphipathic helix. However, several binding assays including our own (vide infra) indicate that extension of the Mad1−SID increases the affinity for PAH2 (*20*, *21*), possibly by additional intermolecular interaction mediated by conserved residues outside the minimal binding motif.

Here, we elaborate further on the structural details of the Mad−Sin3 interaction by reporting the results of a binding study, a high-resolution structure, and a dynamics study on the complex between an extended SID of 24 residues of Mad1 and the PAH2 domain of mSin3B, subsequently denoted as PAH2^{B}−SID24. We show that conserved SID residues outside the minimal binding motif, viz., Met7 and Glu23, interact with PAH2 and thus contribute to the binding affinity, specifically for the Mad family.

EXPERIMENTAL PROCEDURES

Sample Preparation. All NMR studies were performed using a protein construct of 105 residues (denoted as PAH2^{B}) corresponding to residues 148−252 of the long variant of Mm. mSin3B (SpTrEMBL accession number Q62141) and a chemically synthesized polypeptide of 24 residues (denoted as SID24) corresponding to residues 5−28 of Hs. Mad1 (SwissProt accession number Q05195). Cloning, expression, and purification of the PAH2^{B} domain were done as described before (*23*). Uniformly ^{15}N/^{13}C-labeled PAH2^{B} was prepared using [^{15}N]NH$_4$Cl and [^{13}C$_6$]glucose as sole nitrogen and carbon sources. NMR[1] samples contained a 1.3 mM 1:1 complex of ^{13}C/^{15}N double-labeled PAH2^{B} and unlabeled SID24 in a buffer of 50 mM KH_2PO_4/K_2HPO_4 (pH 6.3) and H_2O/^2H_2O (95%/5%), using the protease inhibitor Pefabloc and trace NaN_3 as preservative. The 1:1 stoichiometry of the PAH2−SID interaction was confirmed on the basis of both the results of titrating SID to an NMR sample of free PAH2 (*23*) and the agreement of fit of the experimental SPR data with a 1:1 stoichiometry (data not shown). Samples with free PAH2^{B} and PAH2^{B} in complex with the 13-residue minimal SID were prepared as described before (*23*). Constructs of Hs. Mad1 SIDs of different lengths were fused to the GB1 domain of streptococcal protein G as described earlier (*22*) and were used in the SPR measurements.

Surface Plasmon Resonance Interaction Studies. SPR experiments were performed using a BIAcore 2000 biosensor instrument. Sensor chips and protein coupling chemicals were purchased from Biacore AB (Uppsala, Sweden). Proteins were coupled to the sensor chips by procedures recommended by the manufacturer using EDC and *N*-hydroxysucccinimide for activation of carboxylic groups of the sensor chips, followed by reaction of the protein ligand and finally blocking the excess of activated groups by reaction with 1 M ethanolamine. The immobilization level was optimized for kinetic measurements; the maximal amount of bound analyte (R_{max}) was kept low to minimize mass transport limitation effects on the binding curves and varied between 46 and 128 resonance units. Kinetic measurements were performed at 25 °C with a flow rate of 50 μL/min in HBS, pH 7.4.

Table 1: Binding Affinity of Mad1−SID for the PAH2 Domain of mSin3B

Mad1−SID	sequence	K_D (μM)
5−20	VRMNIQMLLEAADYLE	1.4 ± 0.6
5−24	VRMNIQMLLEAADYLERRER	0.4 ± 0.1
5−28[a]	VRMNIQMLLEAADYLERREREAEH	0.3 ± 0.2
5−35	VRMNIQMLLEAADYLERREREAEHGYASML	0.2 ± 0.1

[a] The Mad1−SID construct used for the PAH2^{B}−SID24 complex.

Interaction of the PAH2 domain of mSin3B with the four Mad1/GB1 constructs was measured in duplicate in two independent manners. In the first approach, mSin3B was immobilized, and the binding of the Mad1/GB1 constructs with variable Mad1−SID length was measured during 5 min at 10 different concentrations. Ligand and analyte were reversed in the second approach. Mad1/GB1 constructs were immobilized, and the binding of 10 different concentrations of mSin3B was measured for 5 min. Regeneration of the sensor surface was performed with 50 mM HCl during 3 min. Interactions were also measured on sensor surfaces without immobilized protein as negative controls.

Equilibrium was reached within 30 s for all measured interactions. Steady-state binding kinetics was applied to calculate the binding constant of the interactions. At equilibrium, the relationship between response and concentration is defined as $R_{eq} = K_A \cdot \mathrm{conc} \cdot R_{max}/[1 + K_A \cdot \mathrm{conc} \cdot n]$. R_{eq} corresponds to the steady-state value of a particular concentration of analyte, K_A is the association constant (in M^{-1}), R_{max} is the maximum amount of bound analyte, and n is the number of independent ligand binding sites. The Kinetic Evaluation software of the manufacturer was used to generate overlay plots of 10 concentrations of analyte, to determine R_{eq} values for all concentrations corrected for the negative control responses, and to calculate the dissociation constant K_D (in M). Two independent values of the dissociation constants were calculated for the interaction of mSin3B with four Mad1−SID constructs. Average values are shown in Table 1.

NMR Spectroscopy. All NMR experiments were collected at 20.0 °C on a sample with ^{13}C/^{15}N double-labeled PAH2^{B} and unlabeled SID24. The NMR experiments were carried out on Varian Unity Inova 500, 600, 750, and 800 MHz spectrometers. The data were processed using the NMRPipe suite (*24*) and analyzed using XEASY (*25*). Assignment of PAH2^{B} was based on the assignment of PAH2^{B} in complex with the minimal SID of 13 residues (*22*, *23*). Confirmation of the assignments was obtained using 3D HNCA, HNCACB, CBCACONH, (H)CCH-TOCSY, ^{15}N NOESY-HSQC, and aliphatic ^{13}C NOESY-HSQC spectra. Assignment of the extended SID was performed using the sequential assignment

---

[1] Abbreviations: 2D, two dimensional; 3D, three dimensional; EDC, *N*-ethyl-*N*′-(diethylaminopropyl)carbodiimide; ITC, isothermal titration calorimetry; NMR, nuclear magnetic resonance; NOE, nuclear Overhauser effect; MD, molecular dynamics; RMSD, root mean square deviation; SPR, surface plasmon resonance.

approach (*26*) using a 2D ^{13}C/^{15}N double-filtered NOESY and a 3D doubly sensitivity enhanced ^{13}C/^{15}N-filtered TOCSY-TOCSY (*27*), which was necessary to solve all overlap in the conventional 2D X-filtered TOCSY due to the high redundancy in amino acid composition.

Distance restraints for structure calculations were obtained from 3D ^{15}N NOESY-HSQC, aliphatic ^{13}C NOESY-HSQC, aromatic ^{13}C NOESY-HSQC, and 2D ^{13}C/^{15}N double-filtered NOESY experiments. Intermolecular NOEs were distinguished from intramolecular NOEs using a 3D (^{13}C-edited, ^{13}C/^{15}N-filtered)-HMQC-NOESY and a (^{15}N-edited, ^{15}N/^{13}C-filtered)-HSQC-NOESY. The NOE mixing time in all NOESY experiments was set to 100 ms. To determine changes in the ^{13}C, ^{15}N ,and ^{1}H chemical shifts of the side chain amide groups of Asn and Gln, HNCO experiments optimized for NH_2 moieties were recorded on samples containing the PAH2^{B}−SID13 and PAH2^{B}−SID24 complexes.

The ^{15}N−T_1, ^{15}N−$T_{1\rho}$, and {^{1}H}−^{15}N NOE experiments were recorded at 20.0 °C at 11.7 T. All experiments were recorded in an interleaved manner and in duplicate. Relaxation delays for the PAH2^{B}−SID24 complex were 16, 96, 160, 256, 512, 640, 800, and 1024 ms for the T_1 experiment and 16, 32, 48, 80, 96, 112, and 128 ms for the $T_{1\rho}$ experiment. For the PAH2^{B}−SID13 complex, relaxation delays were 16, 96, 256, 400, 608, 800, and 1024 ms for the T_1 experiment and 16, 32, 48, 64, 80, 96, and 128 ms for the $T_{1\rho}$ experiment. The {^{1}H}−^{15}N NOE values were derived from experiments using 3 s of either on- or off-resonance irradiation with a recycle delay of 1.5 s and an additional 10 s delay after each complex point.

Structure Calculations and Refinement. The NOE peak volumes were converted into distance ranges by normalization against peak volumes that were calibrated to known distances and then overestimated 2-fold. Distance restraint ranges used lower limits of 0 Å and upper limits of 2.8, 3.5, 5.0, or 7.0 Å. Chemical shifts of C$^{\alpha}$ for PAH2 and H$^{\alpha}$ for the SID were used to derive a set of 140 dihedral angle restraints for the backbone angles ϕ and ψ using the program CSI version 2.0 (*28*). An initial set of 200 NMR structures was calculated using a Cartesian-space simulated annealing protocol in X-PLOR version 3.851 (*29*). To improve local geometry and electrostatics, 106 lowest energy structures were then refined in water using a restrained molecular dynamics protocol under a CHARMM22 force field (*30*). Briefly, the unrefined structures are solvated in a TIP3 water box, neutralized, and energy minimized, followed by 3 ps of restrained MD. The initial temperature of the system is set to 300 K and then cooled to 100 K. Force constants for experimental restraints are gradually lowered from 50 to 25 kcal mol^{-1} Å^{-2} and from 200 to 80 kcal mol^{-1} Å^{-2} for NOE and dihedral restraints, respectively. The resulting structures are energy minimized in 250 steps. Of these resulting structures, the 30 lowest energy structures with no distance restraint violations >0.5 Å and dihedral angle violations >5° were selected to form the final ensemble. Structures were analyzed using the programs PROCHECK-NMR (*31*) and WHAT-IF (*32*).

Relaxation Data Analysis. Peak intensities were extracted from the spectra by fitting peaks using the nlinLS module of NMRPipe (*24*). Errors in peak heights were estimated by the root mean square of the noise level. The longitudinal and transverse relaxation rates were calculated by fitting the extracted intensities to a monoexponential decay using the modelXY module of NMRPipe. Errors (1σ confidence limits) were estimated from 21 Monte Carlo simulations. In a conservative approach, all errors for R_1, $R_{1\rho}$, and NOE were estimated to be at least 4% to prevent falsely attributed contributions of internal motions or exchange. The global diffusion tensor was determined using the program TENSOR 1.1 (*33*), resulting in an isotropic diffusion tensor with a global rotation correlation time of 11.2 ns for the PAH2^{B}−SID24 complex and 9.9 ns for the PAH2^{B}−SID13 complex. We used the lowest energy structure and a subset of the R_1 and $R_{1\rho}$ values composed of residues that (i) do not overlap, (ii) have NOE values >0.55, indicating that internal motion of these residues is limited, (iii) have $R_{1\rho}$ within 1 SD from the mean value, indicating that chemical exchange contribution to $R_{1\rho}$ is absent or very small. Although the $R_{1\rho}/R_1$ ratios of the extended SID complex suggest some anisotropy of the diffusion tensor, this effect could not statistically significantly be discriminated from an isotropic model. Subsequently, the R_1, $R_{1\rho}$, and NOE values served as input for the program Modelfree 4.15 (*34*, *35*) to extract parameters describing the internal motions in the model-free approach (*36*−*38*). After model selection, model parameters and the global rotation correlation time (τ_c) were optimized.

RESULTS

Binding. To investigate the effect of extension of the SID on binding affinity, we performed SPR measurements on four different Mad1−SID constructs extended at the C-terminus (Mad1−SID 5−20, 5−24, 5−28, and 5−35). The results are listed in Table 1 and show that extension with the charged residues 21−24 (RRER) increases affinity approximately 5-fold, suggesting an electrostatic interaction between this part of the SID and PAH2. Residues 25−35 do not seem to significantly contribute to binding affinity as constructs SID5−28 and SID5−35 have similar binding affinities compared to SID5−24.

Using ITC measurements Brubaker et al. (*21*) found a K_D of ~0.029 μM for SID6−21 and ~0.015 μM for SID1−35 binding the PAH2 domain of mSin3A, values that are significantly lower when compared to those of mSin3B. We speculate that these differences are most likely caused by the different methods used, since the structure of PAH2^{A}−SID16 shows only little differences with the PAH2^{B}−SID13 and PAH2^{B}−SID24 structures (vide infra). Unfortunately, Brubaker et al. do not provide experimental details regarding the ITC measurements. Nevertheless, both studies clearly show that despite the relative differences in the values of the K_D an extension of SID yields a higher affinity.

Structure. The structure of the complex between the extended 24-residue SID and PAH2 was determined using high-resolution multidimensional heteronuclear NMR. Analysis of edited- and filtered-NOESY experiments revealed 11 new intermolecular NOEs between PAH2 and residues in the extension part of the SID, such as between the ϵ-methyl group of Met7 and the side chain β-protons of Asn156 and Gln225 (cf. Figure 1). In total, 1762 unique distance restraints (Table 2) and 140 dihedral angle restraints for the backbone angles ϕ, ψ were used to calculate the solution structure of this complex. A stereoview of the ensemble of structures is

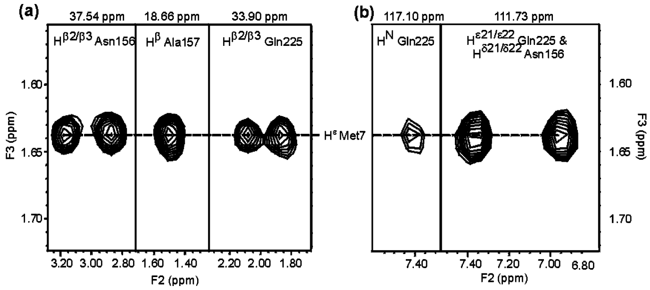

FIGURE 1: New intermolecular NOEs in the extended PAH2^B−SID24 complex. (a) Selected strips from the 3D (^{13}C-edited, ^{13}C/^{15}N-filtered)-HMQC-NOESY spectrum and (b) selected strips from the 3D (^{15}N-edited, ^{15}N/^{13}C-filtered)-HSQC-NOESY spectrum. Frequencies in the F_1 dimension and the assignment of the peaks in the F_2 dimension are given at the top of each strip. Shown in (a) are the peaks corresponding to the NOE transfer from the side chain β-protons of PAH2 residues Asn156, Ala157, and Gln225 to the ϵ-methyl group of Met7 in the SID. Shown in (b) are the peaks corresponding to the NOE transfer from the backbone amide proton of Gln225 and the side chain amide protons of residues Asn156 and Gln225 in PAH2 to the ϵ-methyl group of Met7 in the SID.

Table 2: Structural Statistics for the PAH2^B−SID24 Complex

(A) Restraint Information	
total no. of distance restraints	1762
intra-PAH2 (intraresidual/sequential/medium/long)	1324 (557/347/296/123)
intra-SID (intraresidual/sequential/medium/long)	312 (155/83/74/0)
intermolecular	126
dihedral angle restraints	140
(B) Average RMS Deviation from Experimental Restraints	
all distance restraints (Å)	0.056 ± 0.002
all dihedral angle restraints (deg)	0.58 ± 0.01
(C) Pairwise Cartesian RMS Deviation (Å)	
ordered backbone heavy atoms	0.77 ± 0.12
ordered all heavy atoms	1.74 ± 0.17
global backbone heavy atoms	2.87 ± 0.61
global all heavy atoms	3.73 ± 0.56
(D) Ramachandran Quality Parameters (%)	
residues in most favored regions	84.3
residues in allowed regions	12.1
residues in additionally allowed regions	2.6
residues in disallowed regions	1.1
(E) Abnormalities Found in Structural Checks	
abnormally short interatomic distances	3
unsatisfied H-bond acceptors (buried)	4
unsatisfied H-bond donors (buried)	12
(F) Average RMS Deviation from Current Reliable Structures (RMS *Z*-Scores, Null Deviation = 1)	
bond lengths	1.013
bond angles	1.296
ω angle restraints	1.451
side chain planarity	1.113
improper dihedral distribution	1.007
inside/outside distribution	1.001
(G) Average Deviation from Current Reliable Structures (*Z*-Scores, Null Deviation = 0)	
second generation packing quality	−2.157
Ramachandran plot appearance	−3.354
χ_1/χ_2 rotamer normality	−2.092
backbone conformation	−1.658

Table 3: Analysis of Intermolecular Interactions Involving PAH2-Lys165

ion pair	interaction type[a]	*N* (%)[b]
PAH2-Lys165−SID-Glu23	hydrogen bonded	18 (60)
	N−O bridge	4 (13)
	long-range ion pair	8 (27)
PAH2-Lys165−SID-Glu20	hydrogen bonded	3 (10)
	N−O bridge	0 (0)
	long-range ion pair	27 (90)

[a] Interaction in an ion pair is classified into hydrogen bonded, N−O bridges, or long-range ion pairs, depending on their geometry. Criteria for hydrogen bonds (D−H···A) were a maximum distance r(H,A) of 2.5 Å and a maximum angle θ(D−H−A) of 90°. Interaction is defined as an N−O bridge when r(N,O) < 4.0 Å; otherwise, it is classified as a long-range ion pair (*39*). [b] The number of conformers in which the specified interaction type is observed. The percentage of all conformers in the ensemble is shown in parentheses.

presented in Figure 2a. Statistical data for the ensemble are reported in Table 2. All structures contain neither distance violations >0.5 Å nor dihedral angle violations >5° from experimental data. The pairwise heavy backbone atom RMSD is 0.8 Å for the ordered parts of the structure (residues 152−189 and 202−227 for PAH2 and residues 7−24 for the SID), while the pairwise all heavy atom RMSD is 1.7 Å for the same residues, indicating a well-defined ensemble. The Ramachandran plot displays 84% of the residues in most favored regions and 15% in additionally allowed regions.

The complex forms a wedged helical bundle in which the amphipathic helix of the SID is located between helices α1 and α2 of the four-helix bundle of the PAH2 domain at an angle of ∼45° with respect to α2. Residues 152−167, 172−189, 202−212, and 217−226 of PAH2 form the four helices, α1, α2, α3, and α4, of the four-helix bundle. Residues 168−171 and 213−216 fold into turns, and residues 190−201 form a large loop between helix α2 and helix α3. Residues 233−252 were not included in the structure calculation as NMR data for this highly flexible region (vide infra) did not give any indication of secondary structure. Residues 9−24 of the SID fold as an α-helix, with its hydrophobic residues intensively contacting the hydrophobic pocket of PAH2.

To compare the structure of PAH2^B−SID24 with our previous structure of PAH2^B−SID13, a structural superposition was made using the lowest energy structures (Figure 2b). The heavy backbone atom RMSD for the ordered regions is 1.2 Å, and the heavy all-atom RMSD is 2.0 Å for the same regions, similar to the values for the ensemble of PAH2^B−SID24 structures. As these two structures are highly similar, we refer to Spronk et al. (*22*) for a detailed description of the fold and the hydrophobic interactions stabilizing the complex. Here, we will focus on the structural role of residues located outside the previously defined minimal binding motif.

At the C-terminal end of the Mad minimal binding motif, there are eight additional residues: RREREAEH (residues 21−28). Charged residues 21−24 form a solvent-exposed extension of the SID helix comprising almost two helical turns. These residues were identified in our binding study as responsible for a 5-fold increase in binding affinity. Our structure shows that this increase is due to the electrostatic interaction between the intermolecular ion pair formed by SID-Glu23 and PAH2-Lys165 (Figure 2c). Table 3 summarizes an analysis of this ion pair in the ensemble of conformers obtained by discriminating between a hydrogen bond interaction, a N−O bridge, and a long-range electrostatic interaction (*39*). The results show that in 60% of the conformers Lys165 is hydrogen bonded to Glu23. Further-

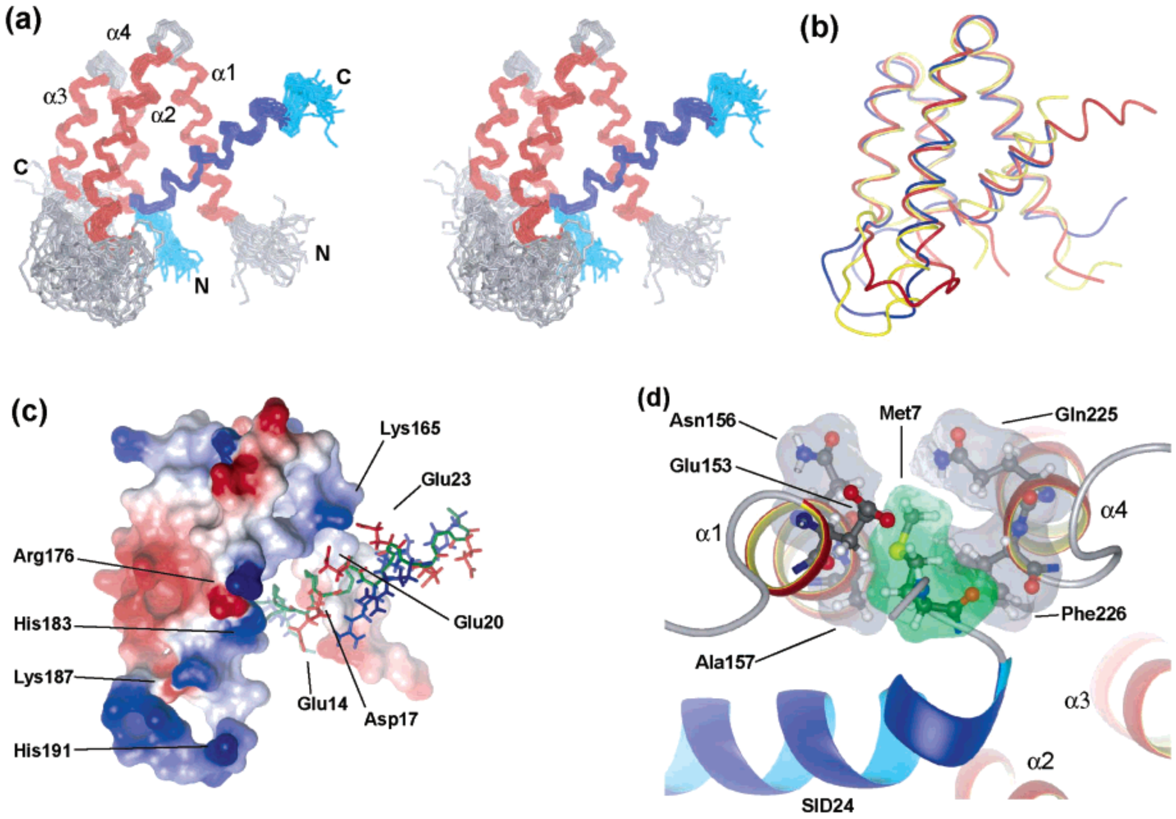

FIGURE 2: (a) Stereo diagram of the structural ensemble of 30 structures of the PAH2^B−SID24 complex. Helices of PAH2^B are shown in red, the helix of the SID is shown in blue; coil and turn regions are shown in gray for PAH2^B and in cyan for the SID. (b) Structural superposition of the lowest energy structures of the PAH2^B−SID13 (blue; PDB code 1E91), PAH2^B−SID24 (red; PDB code 1PD7), and PAH2^A−SID16 (yellow; PDB code 1G1E) complexes. All structures were superposed on the PAH2 domain. (c) Additional electrostatic interactions between PAH2^B-Lys165 and SID-Glu23. PAH2^B is shown in surface representation with color coding according to electrostatic potential; the SID is shown in stick representation with its charged residues shown (for both molecules with color coding: blue = positively charged, red = negatively charged). (d) Additional interactions between SID-Met7 and residues in α1 and α4. The SID helix is shown in blue-cyan; the PAH2^B helices are in red-yellow. The contact surface of the PAH2 residues is shown in gray; the contact surface of Met7 is shown in green. This figure was prepared using MOLMOL (*42*).

more, Lys165 also forms an intermolecular ion pair with SID-Glu20, although this interaction is mainly long range.

Figure 2c displays a surface representation of the PAH2 domain color coded according to the electrostatic potential, showing that helix α2 and part of the loop, α2 to α3, are mainly positively charged due to the presence of Arg176, His183, Lys187, and His191. The SID contains a negatively charged rim formed by residues Glu14, Asp17, and Glu20, resulting in a network of long-range electrostatic interactions between these residues. Other charged residues in the C-terminal extension, residues Arg21 and Arg22 and residues Arg24−His28 point away from the interaction surface into the solvent.

The three additional residues at the N-terminus, residues 5−7 (VRM), do not form an extension of the SID helix; instead, the backbone adopts a mainly extended conformation protruding from the base of PAH2. Consistent with the intermolecular NOEs observed for SID-Met7, its side chain is inserted between the backbone of α1 and α4 in a hydrophobic pocket formed by Glu153, Asn156, and Ala157 in helix α1 and Gln225 and Phe226 in helix α4 (Figure 2d).

Another additional interaction was found for residue SID-Met11, which is in the minimal binding motif. New intermolecular NOEs were observed, indicating that the side chain of SID-Met11 contacts residues Glu153, Phe154, and Ala157 in helix α1 (data not shown). Comparison of the observed intermolecular NOEs in the PAH2^B−SID24 and PAH2^B−SID13 complexes yielded no further significant differences.

Dynamics. We performed ^{15}N relaxation measurements to probe the dynamical behavior of the PAH2 domain when complexed to the extended SID of 24 residues and the minimal SID of 13 residues. We recorded the $^{15}\text{N}-T_1$, $^{15}\text{N}-T_{1\rho}$, and $\{^1\text{H}\}-^{15}\text{N}$ NOE experiments and used the model-free approach (*36*−*38*) as implemented in the program Modelfree 4.15 (*34*, *35*) to calculate dynamical parameters describing the global rotational diffusion of the complex and local internal motions of the backbone of PAH2.

For the PAH2^B−SID24 complex, reliable data could be extracted for 77 out of 102 non-proline residues; for the PAH2^B−SID13 complex we obtained data for 69 out of 102 residues. The global rotational diffusion tensor was determined to be isotropic with optimized values for the global correlation time, τ_c, of 11.5 ± 0.1 and 10.0 ± 0.1 ns for the PAH2^B−SID24 and the PAH2^B−SID13 complex, respectively. These values are higher than expected for a typical protein of similar size but just within the upper limit (*40*). A possible explanation for this deviation is a reduction of the rotational diffusion caused by the unstructured flexible C-terminal tail and the large flexible loop between α2 and α3 in PAH2 indicated by low values for the NOE (average 0.35 ± 0.09 for the loop and −0.6 ± 0.2 for residues 233−

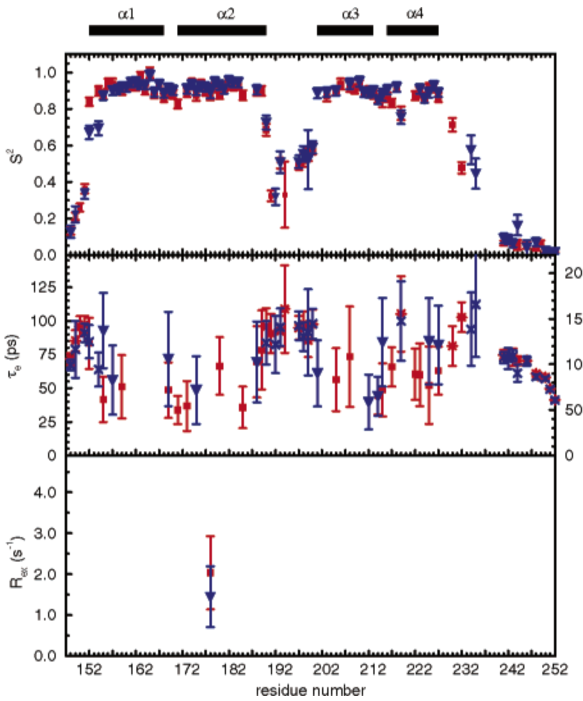

FIGURE 3: Results of the ^{15}N relaxation analysis for the PAH2 domain using the model-free approach. Shown are the dynamical parameters of PAH2 in the PAH2^B–SID24 complex (red squares) and in the PAH2^B–SID13 complex (blue triangles). The top panel displays the generalized order parameter squared (S^2), the middle panel shows the rotational correlation times (τ_e) for fast internal motions (red squares for PAH2^B–SID24 and blue triangles for PAH2^B–SID13; axis shown on the left-hand side) and for slow internal motions (red stars for PAH2^B–SID24 and blue crosses for PAH2^B–SID13; axis shown on the right-hand side), and the lower panel presents the chemical exchange contribution R_{ex}. The secondary structure of the PAH2^B domain is shown in the top of the figure with helices represented as black rectangles.

252) and the order parameter (average 0.55 ± 0.18 for the loop and 0.05 ± 0.02 for residues 233–252).

Model-free analysis describes local motions using three dynamical parameters: the square of the generalized order parameter S^2, which is correlated to the amplitude of the motion, the effective correlation time of the internal motions τ_e, which indicates the time scale of internal motions, and the chemical exchange contribution R_{ex}, which is indicative of motions on a microsecond to millisecond time scale. These parameters are presented in Figure 3 for both the PAH2^B–SID24 and the PAH2^B–SID13 complex. The four helices and the two turns, α1 to α2 and α3 to α4, have average S^2 values of around 0.9, indicating that these regions form rigid structures. The loop between α2 and α3 and the N- and C-termini are the highly flexible parts of the domain with average S^2 values in the range of 0.2–0.5, consistent with the higher local RMSD for these regions in the ensemble.

Nineteen residues for PAH2^B–SID24 and 11 residues for PAH2^B–SID13 show contributions from local internal motions on a time scale of 30–150 ps. Mostly, these residues have surface-exposed side chains. One residue, Phe178 in α2, requires a small chemical exchange contribution in both complexes (2.0 ± 0.9 s^{-1} for PAH2^B–SID24 and 1.4 ± 0.8 s^{-1} for PAH2^B–SID13). Strikingly, Leu219 in helix α4 shows a complex dynamical behavior with a lower than average S^2 (~0.76) and internal motions on a fast and slow (~1.5 ns) time scale. Furthermore, residues Lys163 in the PAH2^B–SID24 complex and Lys165 in both complexes in helix α1 display a significantly higher than average S^2.

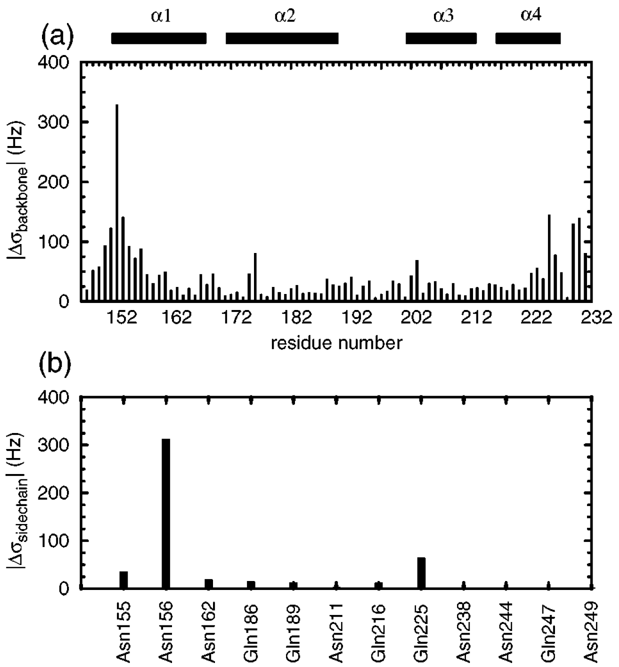

FIGURE 4: Absolute chemical shift differences between the PAH2^B–SID24 and PAH2^B–SID13 complexes for backbone resonances (a) and selected side chain resonances (b). The difference in chemical shift was calculated as the vector displacement in hertz between the two complexes of the H^N, N, and C^α resonances (a) or the C^γ, N^δ, $H^{\delta21}$, and $H^{\delta22}$ for the asparagine amide group and the C^δ, N^ϵ, $H^{\epsilon21}$, and $H^{\epsilon22}$ for the amide group of glutamines (b). The secondary structure of the PAH2^B domain is shown in the top of the figure with helices represented as black rectangles.

With the exception of the N-terminal region of helix α1, the dynamics of PAH2 in the PAH2^B–SID13 and PAH2^B–SID24 complexes is highly similar, as expected since the fold of PAH2 is identical. Dramatic changes are observed for residues 152 and 154 in the first turn of helix α1, which show a large increase in S^2 of about 0.2 unit for the PAH2^B–SID24 compared to PAH2^B–SID13. While in the PAH2^B–SID13 complex these residues are flexible and have internal motions on a fast and a slow time scale, in the PAH2^B–SID24 complex they are significantly less flexible and do not show internal motions on a slow time scale. This is in close agreement with additional intermolecular interactions observed in the PAH2^B–SID24 complex between Met7 and Met11 with the N-terminal region of α1, which will evidently constrain the flexibility of the backbone. These data, together with the NOE relaxation data of the free PAH2 domain (*22*), suggest that the flexibility of the first two turns of α1 in the free PAH2 is necessary to allow the SID to enter the binding pocket. Upon binding, intermolecular interactions between the SID and the N-terminal part of helix α1 "lock" the helix, increasing its rigidity and stability.

Chemical Shift Perturbation. Figure 4 displays the chemical shift differences between the PAH2^B–SID24 and PAH2^B–SID13 complexes for the backbone resonances (Figure 4a) and the side chain amide resonances of asparagines and glutamines (Figure 4b). Consistent with the structural differences between the two complexes, it shows large differences for the first part of helix α1 and the last few residues of α4, with respect to both the backbone resonances and side chain resonances. Especially the backbone resonances of Glu153 and Gln225 and the side chain amides of Asn156 and Gln225 shift dramatically, which is in agreement with the observed new intermolecular contacts between SID-Met7 and these residues. Residues 229−232 also show significant differences in backbone chemical shift, but NOE data did not give any indication of a structural change for these residues.

DISCUSSION

SID-Met7 and SID-Glu23 Contribute to Binding Affinity. We reported a binding study, the solution structure and dynamics of the complex between a 24-residue extended Sin interacting domain of Mad1 and the PAH2 domain of mSin3B. The PAH2^B−SID24 structure shows that extension of the SID does not affect the global fold of PAH2 and preserves the general mode of the SID−PAH2 interaction. However, new intermolecular interactions, both hydrophobic and electrostatic, involving residues in the N- and C-terminal parts of the SID have been identified, i.e., SID-Met7 and SID-Glu23. On the basis of the observed intermolecular NOEs and in agreement with chemical shift perturbation data, SID-Met7 is involved in a hydrophobic interaction with residues in α1 and α4, resulting in an increase in rigidity of the first turn of α1 in accordance with our dynamics data. Furthermore, there is a new electrostatic interaction and intermolecular hydrogen bond involving SID-Glu23 and PAH2-Lys165 in α1 of PAH2, as suggested by both our SPR binding assay and the structural ensemble. Electrostatic interactions are notoriously difficult to prove directly by NMR data. Also in this case, we did not observe intermolecular NOEs or significant changes in chemical shifts involving PAH2-Lys165. However, the use of a water refinement protocol that explicitly treats electrostatic forces will correct for this lack in experimental restraints. In fact, the CHARM22 protocol has been proven to yield more accurate and precise NMR structures with both significantly improved electrostatic and hydrogen bond donor and acceptor properties (*30*).

Apart from the crucial role for PAH2-Lys165 in mediating intermolecular contacts, PAH2 residues Glu153, Asn156, Ala157, Gln225, and Phe226 also contribute to the additional intermolecular interactions.

Comparison of PAH2^B−SID24 with PAH2^A−SID16. Figure 2b shows the superposition of the PAH2^B−SID24 structure and the PAH2^A−SID16 structure (*21*). The PAH2^B and PAH2^A sequences have an overall sequence identity of 61%, which increases to 75% for the structured regions (residues 152−189 and 202−226). The α2 to α3 loop shows most sequence diversity and is three residues longer in PAH2^A compared to PAH2^B. Overall the fold is highly similar. There are, however, three striking differences: (i) helix α2 is extended by almost two turns in PAH2^A−SID16; (ii) SID-Met7 does not interact with α1 and α4 in PAH2^A−SID16; (iii) SID-Glu20 is identified as the key interaction partner for Lys315 in PAH2^A−SID16, corresponding to Lys165 in PAH2^B.

While helix α2 in PAH2^B−SID24 is 18 residues long and extends from Pro172 to Gln189, this helix is extended at its C-terminus in PAH2^A−SID16 to cover 24 residues. Comparison of the corresponding sequence of mSin3B, LHTKGR (residues 190−195), to this C-terminal extension of helix α2 in mSin3A, RNAKEA (residues 340−345), suggests an intrinsic difference as the mSin3A sequence has a higher helix propensity than the mSin3B sequence. Furthermore, our dynamics data clearly indicate that α2 extends to residue 189 and that residues 190−200 form a highly flexible loop. Brubaker et al. (*21*) do not provide detailed information on the dynamics of the PAH2^A domain but do state that the C-terminal part of helix α2 has lower NOE values (in the range of 0.3−0.7), indicating increased flexibility.

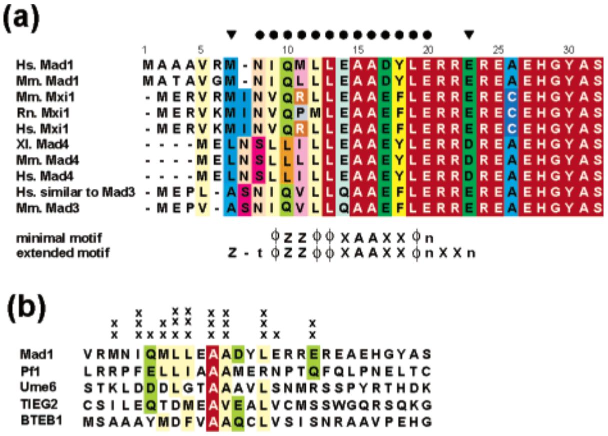

FIGURE 5: (a) Multiple sequence alignment of the Mad family proteins from different species. Numbering in the top row refers to Hs. Mad1. Conserved residues are depicted in red; other colors denote sequence similarities. ● = residues in the minimal binding motif; ▼ = residues showing additional intermolecular interactions. The minimal and extended binding motifs are given below the sequence alignment (written in standard one-letter code; ϕ = bulky hydrophobic residue; X = non-proline residue; Z = large residue with a significant aliphatic component; n = negatively charged residue; t = small residue). (b) Alignment of sequences of the PAH2 binding SIDs of Mad1, Pf1, Ume6, TIEG2, and BTEB1. Conserved residues are depicted in red; other colors denote sequence similarities. The number of crosses above a residue indicates its relative importance in mediating intermolecular contacts with the PAH2 domain for the case of Mad1: XXX = most important, XX = important, and X = less important.

Interaction between SID-Met7 and α1 and α4 of PAH2 is not present in the PAH2^A−SID16 structure. Analysis of the restraint lists of this structure shows that Brubaker et al. did not identify any intermolecular NOEs for Met7. Possibly, Met7 is too flexible to interact, since it is the penultimate residue in the mSin3A complex. Nevertheless, our studies show convincing evidence for this interaction: (i) observation of a number of intermolecular NOEs between Met7 and residues in α1 and α4; (ii) increase in rigidity of the first part of α1 as a result of this interaction; (iii) large chemical shift changes for the involved residues. Furthermore, biochemical data as reported by Eilers et al. (*20*) confirm this interaction. In their two-hybrid assay, extension of the minimal SID (residues 8−20) with Met7 yielded a 1.7-fold increase in reporter activity, clearly suggesting a higher binding affinity. Finally, sequence alignment of the Mad family members in Figure 5a shows that a large hydrophobic residue is conserved at position 7. Furthermore, a small residue with a preference for turns is conserved at position 8, which is crucial to allow proper positioning of Met7.

Previously, Brubaker et al. (*21*) identified the interaction between PAH2^A-Lys315 and SID-Glu20 as a key intermolecular interaction. Mutation of PAH2^A-Lys315 to either Ala or Glu resulted in a significantly reduced binding affinity as measured in a GST pull-down assay using a GST-fused SID as bait for either wild-type or mutant mSin3A. However, a SID consisting of the first 27 residues of Mad1 was used, thus including SID-Glu23. Our structure clearly shows that SID-Glu23 is much closer to, and thus more strongly interacting with, PAH2^B-Lys165 than SID-Glu20. Both in our structure and in their PAH2^A−SID16 structure, SID-Glu20 forms mainly a weak, long-range ion pair with this lysine residue. Therefore, we suggest that SID-Glu23 and not SID-Glu20 is responsible for this key intermolecular interaction.

Extended Binding Motif. The impact of these interactions on binding affinity when compared to the minimal binding sequence can be estimated to be an increase of approximately 10-fold based on our interaction study and that of Eilers et al. (*20*), in which the former shows a 5-fold increase caused by the interactions involving Glu23 and the latter suggests that Met7 is responsible for an almost 2-fold increase in binding affinity. Therefore, we propose to extend the sequence motif to describe the Mad−Sin3 interaction more accurately. The sequence alignment of the Mad family proteins shown in Figure 5a shows that a negative charge is conserved at the position of Glu23 and a bulky aliphatic residue is conserved at the position of Met7 together with a small turn residue at the position of Asn8, which is crucial because of its structural role in allowing the SID backbone to bend in the direction of α1 and α4. For Mad4 proteins there are two small turn residues, Asn and Ser, that could allow Leu to take the role of Mad1-Met7 in mediating hydrophobic contacts with α1 and α4. In the Mxi1 proteins there is an Ile positioned between the Asn and Met, suggesting that in this case Ile rather than Met is involved in contacts with the protein.

This high degree of conservation suggests that the binding mode described here for the Mad1−Sin3 interaction is also valid for the other Mad family proteins. The extended sequence motif is ZtϕZZ$\phi\phi$XAAXXϕnXXn, where ϕ denotes any bulky hydrophobic residue, X is any non-proline residue, Z denotes any hydrophobic or polar/charged residue with a significant aliphatic component, t represent a small turn residue, and n designates a negatively charged residue.

The resulting view is that the hydrophobic face of the SID formed by Ile9, Leu12, Leu13, Ala15, Ala16, and Leu19 provides the basis for interaction with the hydrophobic pocket of PAH2, resulting in a basic level of binding affinity. Other residues, outside this minimal hydrophobic surface, viz., Met7, Met11, Glu23, and to a lesser extent Glu20 and Gln10, provide an additional contribution to affinity. The remaining residues are excluded from the sequence motif as they show only minor involvement in intermolecular contacts. Residues Glu14 and Asp17 participate only in long-range electrostatic interactions, which might not stabilize the complex, as long-range electrostatic interactions are weak and the presence of a water shell could quench the effective electrostatic field even further. However, since a network of electrostatic interactions is possible, involving the four negatively charged residues in the SID and at least four positively charged residues in PAH2, the net effect can be substantial. Additionally, these charges could play a role in complex formation, enhancing the on-rate by long-range electrostatic forces.

The functional role of the 100% conserved EHGYAS sequence is still unclear. One might envisage that the GYASMLP sequence extends the Mad helix described here for another two turns. This will leave the EGYAS sequence too far away from PAH2 for any direct interaction. This is confirmed in the SPR binding assay, in which extension of the SID with this sequence did not affect the binding affinity significantly, in agreement with earlier reports (*12*, *20*). Thus, we speculate that it plays an important architectural role in the complete Mad protein or might interact with an unidentified partner.

Implications for Other PAH2-Interacting SIDs. The extended sequence motif not only is a more accurate description of the interaction of proteins from the Mad family with PAH2 but also is specific for this family. Although other repressor proteins also have PAH2-interacting SID sequences that can be modeled as an amphipathic helix, there is no clear homology between the SIDs, as can be inferred from an alignment of the extended Mad−SID with the SIDs of Pf1, Ume6, TIEG2, and BTEB1 (Figure 5b). Homology between these sequences is restricted to a short minimal core sequence, ϕ-ϕ-X-A-A-X-X-ϕ, with only one strictly conserved residue (Ala15). Thus, the extended sequence motif discriminates the Mad family proteins from other classes of PAH2-interacting proteins.

Furthermore, as residues that mediate important intermolecular interactions for the Mad proteins, such as Ile8 and the newly identified Glu23 and Met7, do not show any obvious similarities in Pf1, Ume6, TIEG2, or BTEB1, we suggest that these proteins show significant differences in their precise binding modes, either interacting via the minimal core only or, analogous to the Mad proteins, involving additional residues outside this minimal motif to mediate intermolecular interactions. In fact, a recent study proposed a completely different model for the TIEG2-SID−PAH2 interaction based on molecular dynamics simulations and biochemical data (*41*). In this model, the TIEG2-SID is not wedged in the PAH2 four-helix bundle, but instead its helix is bound in a parallel manner to the outside surface formed by helix α1 and α2 by both hydrophobic and electrostatic interactions. Notably, the residues involved in crucial intermolecular contacts do not correspond to the minimal motif.

CONCLUSIONS

In conclusion, NMR data, binding studies, dynamics data, sequence alignment, and previously described binding studies point to additional interactions between an extended Mad−SID and the PAH2 domain of mSin3. Furthermore, SID-Glu23 is involved in a key intermolecular interaction with PAH2^B-Lys165, previously attributed to SID-Glu20. This has led us to propose an extended sequence motif showing that residues outside the hydrophobic core of the SID interact with PAH2 and modulate binding affinity in a manner specific for the Mad family.

ACKNOWLEDGMENT

We thank Jan Aelen for technical assistance and purification of the labeled proteins and Tine Walma for proofreading the manuscript.

REFERENCES

1. Hassig, C. A., Fleischer, T. C., Billin, A. N., Schreiber, S. L., and Ayer, D. E. (1997) Histone deacetylase activity is required for full transcriptional repression by mSin3A, *Cell 89*, 341−347.
2. Laherty, C. D., Yang, W. M., Sun, J. M., Davie, J. R., Seto, E., and Eisenman, R. N. (1997) Histone deacetylases associated with the Sin3 corepressor mediate Mad transcriptional repression, *Cell 89*, 349−356.
3. Zhang, Y., Iratni, R., Erdjument-Bromage, H., Tempst, P., and Reinberg, D. (1997) Histone deacetylases and SAP18, a novel polypeptide, are components of a human Sin3 complex, *Cell 89*, 357−364.
4. Ayer, D. E. (1999) Histone deacetylases: transcriptional repression with SINers and NuRDs, *Trends Cell Biol. 9*, 193−198.
5. Ahringer, J. (2000) NuRD and SIN3: histone deacetylase complexes in development, *Trends Genet. 16*, 351−356.
6. Zhang, Y., Sun, Z. W., Iratni, R., Erdjument-Bromage, H., Tempst, P., Hampsey, M., and Reinberg, D. (1998) SAP30, a novel protein conserved between human and yeast, is a component of a histone deacetylase complex, *Mol. Cell 1*, 1021−1031.
7. Alland, L., David, G., Hong, S. L., Potes, J., Muhle, R., Lee, H. C., Hou H., Chen, K., and DePinho, R. A. (2002) Identification of mammalian Sds3 as an integral component of the Sin3/histone deacetylase corepressor complex, *Mol. Cell. Biol. 22*, 2743−2750.
8. Fleisher, T. C., Yun, U. J., and Ayer, D. E. (2003) Identification and characterization of three new components of the mSin3A Corepressor complex, *Mol. Cell. Biol. 23*, 3456−3467.
9. Murphy, M., Ahn, J., Walker, K. K., Hoffman, W. H., Evans, R. M., Levine, A. J., and George, D. L. (1999) Transcriptional repression by wild-type p53 utilizes histone deacetylases, mediated by interaction with mSin3A, *Genes Dev. 13*, 2490−2501.
10. Nan, X., Ng, H. H., Johnson, C. A., Laherty, C. D., Turner, B. M., Eisenman, R. N., and Bird, A. (1998) Transcriptional repression by the methyl-CpG-binding protein MeCP2 involves a histone deacetylase complex, *Nature 393*, 386−389.
11. Jones, P. L., Veenstra, G. J., Wade, P. A., Vermaak, D., Kass, S. U., Landsberger, N., Strouboulis, J., and Wolffe, A. P. (1998) Methylated DNA and MeCP2 recruit histone deacetylase to repress transcription, *Nat. Genet. 19*, 187−191.
12. Ayer, D. E., Lawrence, Q. A., and Eisenman, R. N. (1995) Mad-Max transcriptional repression is mediated by ternary complex formation with mammalian homologs of yeast repressor Sin3, *Cell 80*, 767−776.
13. Schreiber-Agus, N., Chin, L., Chen, K., Torres, R., Rao, G., Guida, P., Skoultchi, A. I., and DePinho, R. A. (1995) An amino-terminal domain of Mxi1 mediates anti-Myc oncogenic activity and interacts with a homolog of the yeast transcriptional repressor SIN3, *Cell 80*, 777−786.
14. Zhou, Z. Q., and Hurlin, P. J. (2001) The interplay between Mad and Myc in proliferation and differentiation, *Trends Cell Biol. 11*, S10−S14.
15. Lüscher, B. (2001) Function and regulation of the transcription factors of the Myc/Max/Mad network, *Gene 277*, 1−14.
16. Grandori, C., Cowley, S. M., James, L. P., and Eisenman, R. N. (2000) The Myc/Max/Mad network of the transcriptional control of cell behavior, *Annu. Rev. Cell. Dev. Biol. 16*, 653−699.
17. Khan, M. M., Nomura, T., Kim, H., Kaul, S. C., Wadhwa, R., Shinagawa, T., Ichikawa-Iwata, E., Zhong, S., Pandolfi, P. P., and Ishii, S. (2001) Role of PML and PML-RARalpha in Mad-mediated transcriptional repression, *Mol. Cell 7*, 1233−1243.
18. Foley, K. P., and Eisenman, R. N. (1999) Two MAD tails: what the recent knockouts of *Mad1* and *Mxi1* tell us about the MYC/MAX/MAD network, *Biochim. Biophys. Acta 1423*, M37−M47.
19. Schreiber-Agus, N., and DePinho, R. A. (1998) Repression by the Mad(Mxi1)-Sin3 complex, *BioEssays 20*, 808−818.
20. Eilers, A. L., Billin, A. N., Liu, J., and Ayers, D. E. (1999) A 13-amino acid amphipathic α-helix is required for the functional interaction between the transcriptional repressor Mad1 and mSin3A, *J. Biol. Chem. 274*, 32750−32756.
21. Brubaker, K., Cowley, S. M., Huang, K., Loo, V., Yochum, G. S., Ayer, D. E., Eisenman, R. N., and Radhakrishnan, I. (2000) Solution structure of the interacting domains of the Mad-Sin3 complex: implications for recruitment of a chromatin-modifying complex, *Cell 103*, 655−665.
22. Spronk, C. A. E. M., Tessari, M., Kaan, A. M., Jansen, J. F. A., Vermeulen, M., Stunnenberg, H. G., and Vuister, G. W. (2000) The Mad1-Sin3B interaction involves a novel helical fold, *Nat. Struct. Biol. 7*, 1100−1104.
23. Spronk, C. A. E. M., Jansen, J. F. A., Tessari, M., Kaan, A. M., Aelen, J., Lasonder, E., Stunnenberg, H. G., and Vuister, G. W. (2001) Letter to the editor: sequence-specific assignment of the PAH2 domain of Sin3B free and bound to Mad1, *J. Biomol. NMR 19*, 377−378.
24. Delaglio, F., Grzesiek, S., Vuister, G. W., Zhu, G., Pfeiffer, J., and Bax, A. (1995) NMRPipe−A multidimensional processing system based on UNIX pipes, *J. Biomol. NMR 4*, 277−293.
25. Bartels, C. H., Xia, T. H., Billeter, M., Güntert, P., and Wütrich, K. (1995) The program XEASY for computer-supported NMR spectral analysis of biological macromolecules, *J. Biomol. NMR 6*, 1−10.
26. Wüthrich, K. (1986) *NMR of proteins and nucleic acids*, Wiley, New York.
27. van Ingen, H., Tessari, M., and Vuister, G. W. (2002) A 3D doubly sensitivity enhanced X-filtered TOCSY-TOCSY experiment, *J. Biomol. NMR 24*, 155−160.
28. Wishart, D. S., and Sykes, B. D. (1994) The ^{13}C chemical shift method. A simple method for the identification of protein secondary structure using ^{13}C chemical shift data, *J. Biomol. NMR 4*, 171−180.
29. Brünger, A. T. (1996) *X-PLOR Version 3.851. A system for X-ray crystallography and NMR*, Yale University Press, New Haven, CT.
30. Spronk, C. A. E. M., Linge, J. P., Hilbers, C. W., and Vuister, G. W. (2002) Improving the quality of protein structures determined by NMR spectroscopy, *J. Biomol. NMR 22*, 281−289.
31. Laskowski, R. A., Rullmann, J. A., MacArthur, M. W., Kaptein, R., and Thornton, J. M. (1996) AQUA and PROCHECK−NMR: programs for checking the quality of protein structures solved by NMR, *J. Biomol. NMR 8*, 477−486.
32. Vriend, G. (1990) WHAT-IF: a molecular modelling and drug design program, *J. Mol. Graphics 8*, 52−56.
33. Dosset, P., Hus, J. C., Blackledge, M., and Marion, D. (2000) Efficient analysis of Macromolecular Rotational Diffusion from Heteronuclear Relaxation Data, *J. Biomol. NMR 16*, 23−28.
34. Mandel, A. M., Akke, M., and Palmer, A. G. (1995) Backbone dynamics of *Escherichia coli* Ribonuclease HI: correlations with structure and function in an active enzyme, *J. Mol. Biol. 246*, 144−163.
35. Palmer, A. G., Rance, M., and Wright, P. E. (1991) Intramolecular motions of a Zn finger DNA-binding domain from Xfin characterized by proton-detected natural abundance ^{13}C heteronuclear NMR spectroscopy, *J. Am. Chem. Soc. 113*, 4371−4380.
36. Lipari, G., and Szabo, A. (1982) Model-free approach to the interpretation of nuclear magnetic resonance in macromolecules 1: Theory and range of validity, *J. Am. Chem. Soc. 104*, 4546−4559.
37. Lipari, G., and Szabo, A. (1982) Model-free approach to the interpretation of nuclear magnetic resonance in macromolecules 2: Analysis of experimental results, *J. Am. Chem. Soc. 104*, 4559−4570.
38. Clore, G. M., Szabo, A., Bax, A., Kay, L. E., Driscoll, P. C., and Gronenborn, A. M. (1990) Deviations from the simple 2-parameter model-free approach to the interpretation of N-15 nuclear magnetic-relaxation of proteins, *J. Am. Chem. Soc. 112*, 4989−4991.
39. Kumar, S., and Nussinov, R. (2002) Relationship between ion pair geometries and electrostatic strengths in proteins, *Biophys. J. 83*, 1595−1612.
40. Engelke, J., and Rüterjans, H. (1999) Recent developments in studying the dynamics of protein structures from 15N and 13C relaxation time measurements, in *Biological Magnetic Resonance. Vol. 17: Structure Computation and Dynamics in Protein NMR* (Krishna, N. R., and Berliner, L. J., Eds.) Kluwer Academic/Plenum Publishers, New York.
41. Pang, Y.-P., Kumar, G. A., Zhang, J.-S., and Urrutia, R. (2003) Differential binding of Sin3 interacting repressor domains to the PAH2 domain of Sin3A, *FEBS Lett. 548*, 108−112.
42. Koradi, R., Billeter, M., and Wüthrich, K. (1996) MOLMOL: a program for display and analysis of macromolecular structures, *J. Mol. Graphics 14*, 51−55.

BI0355645